Anisotropic fluorescence signals retarded dipole-dipole interactions in a thermal atomic cloud

Vyacheslav Shatokhin, ^{1, 2, *} Friedemann Landmesser, ¹ Mario Niebuhr, ¹ Frank Stienkemeier, ¹ Andreas Buchleitner, ^{1, 2} and Lukas Bruder ¹

¹Institute of Physics, University of Freiburg, Hermann-Herder-Str. 3, D-79104 Freiburg, Germany

²EUCOR Centre for Quantum Science and Quantum Computing,

Albert-Ludwigs-Universität Freiburg, Hermann-Herder-Str. 3, D-79104 Freiburg, Germany

(Dated: September 3, 2025)

We experimentally observe and theoretically explain anisotropic multiple quantum coherence signals in the fluorescence from dilute thermal potassium vapors, at room temperature and particle densities $\sim 10^8~{\rm cm}^{-3}$. We identify the retarded part of the geometrically fully resolved inter-atomic, resonant dipole-dipole interaction as the crucial ingredient to theoretically reproduce all qualitative features of the experimental spectra.

Introduction.— In an atomic gas, spontaneous emission from an atom's electronic excited states is affected by dipole-dipole interactions with surrounding atoms, which are mediated by the electromagnetic environment [1–4]. In thermal clouds, one is tempted to argue that the atoms' motion washes out any coherent inter-atomic interactions, such that their fluorescence properties can be considered that of independent particles [5, 6]. However, several publications [7–14] reported multiple quantum coherence (MQC) signals, by ultrafast nonlinear spectroscopy methods. They oscillate at integer multiples $\kappa < 8$ of a single atom's dipole transition frequencies, and are observed at room temperature, down to extremely low particle concentrations $\sim 8 \times 10^6 \text{ cm}^{-3}$ [9]. These observations suggest coherent interactions between at least κ atoms, contradict the above picture of independent atomic emitters, and triggered a hitherto open debate on the origin of the experimental observations. Furthermore, they underpin evidence for non-trivial quantum optical phenomena in thermal many-body systems, with a panoply of potential applications for spectroscopic [15– 17] and quantum information [18–21] purposes.

In our present contribution, we seek to settle the above debate, in a joint effort of theory and experiment. Combining a full-fledged quantum optical treatment of the inter-atomic interaction through the atoms' electromagnetic environment with a faithful description of the vector-valued character of the atomic dipole transitions and some ingredients of disorder physics, we identify a directional anisotropy in the experimentally recorded $\kappa = 1.2 \text{ MQC signal as a hallmark of the dominant far}$ field character of the coherent dipole interaction. This simple observable yields unambiguous experimental evidence for our theoretical model, in which quantum emitters with sufficiently small relative velocities remain coupled by the retarded dipole-dipole interactions, despite the atoms' thermal motion. Our results crucially depend on the accurate account of the internal quantum structure of the degenerate dipole transitions of alkali atoms. Comparing experimental data to our theoretical model's

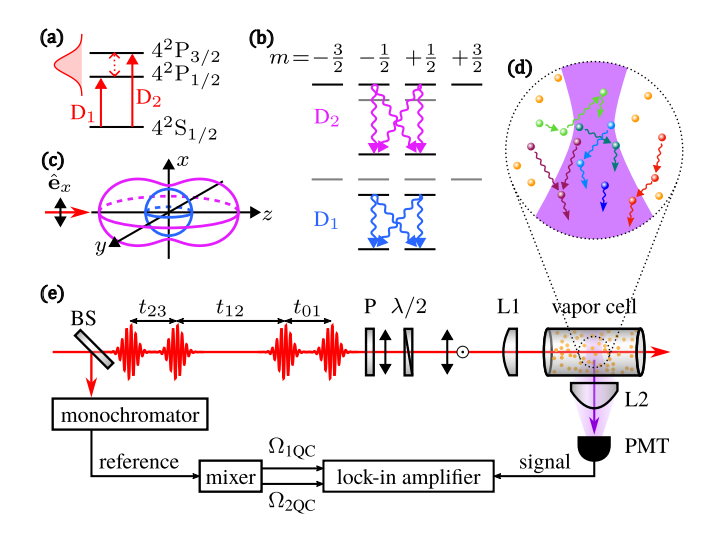


Figure 1. Main ingredients of the experiment: (a) Soild red lines indicate the K atoms' D_1 , D_2 -line transitions [22]; the red dotted arrow the fine structure coherence. (b) Zeeman structure of the D_1 , D_2 transitions, with magnetic quantum numbers m, and fluorescence channels contributing for $\hat{\mathbf{x}}$ -polarized incoming pulses. (c) Associated fluorescence angular distribution; details in [23]. (d) Disordered, thermal vapor where resonant photon exchange (wiggly arrows) is possible for particles with similar velocities (same color). (e) Experimental setup (see main text).

predictions, we can rule out the model of independent emitters, as well as the hypothesis of only electrostatic dipole-dipole interactions.

Experimental setup. — Most aspects of the experimental setup were described previously [9]. Our spectroscopic scheme is based on two-dimensional MQC spectroscopy [10, 11] using the phase modulation technique [14, 24]. Phase-modulated electronic coherences are induced in a potassium (K) vapor (Fig. 1(a)), at $T \approx 295 \,\mathrm{K}$ and particle density $n_0 \approx 5 \times 10^8 \,\mathrm{cm}^{-3}$, and are tracked using $M_{\rm cyc} \gg 1$ excitation/detection cycles. Figure 1(e) shows our experimental scheme for a single cycle. Briefly, four linearly polarized Gaussian pulses,

each with center wavelength $\lambda \approx 768 \,\mathrm{nm}$, energy $\simeq 54 \,\mathrm{pJ}$ and duration $\sigma = 190 \,\mathrm{fs}$, are created at relative times t_i (j = 0, 1, 2, 3) in nested Mach-Zehnder interferometers, and phase modulated using acousto-optical modulators, at frequencies Ω_i , in each interferometer arm [25]. The pulses are focused by lens L1 into a $L = 5 \,\mathrm{cm}$ long alkali vapor cell. The fluorescence light is collected (irrespective of its polarization) by lens L2, and detected by a photomultiplier tube (PMT), over a solid angle of $\approx 0.38 \,\mathrm{sr.}$ The incoming laser polarization with respect to the detection direction (perpendicular to the incoming radiation's wave vector) is controlled with high accuracy by a combination of a linear wire-grid polarizer (P) and a halfwave plate $(\lambda/2)$, set either along $(\hat{\mathbf{x}})$ or perpendicular $(\hat{\mathbf{y}})$ to the detection axis. A lock-in detection scheme [24] allows to extract specific κ contributions from the overall signal [14], by scanning the delay time $\tau := t_{12} \equiv t_2 - t_1$ of the central pulse pair with a mechanical delay line, thus recording a one-dimensional interferogram over the τ axis. We fix the other delays, $t_{01} = t_{23} = 577 \, \text{fs}$, to avoid possible time-ordering artifacts [26, 27] due to the finite pulse duration. The lock-in reference signal is constructed by detecting the modulated interference of the pulses with a monochromator and filtering it at specific frequencies $\Omega_{1QC} = \Omega_2 - \Omega_1 = 2.7 \, \text{kHz}$ and $\Omega_{\rm 2QC} = \Omega_{\rm 1QC} + \Omega_3 - \Omega_0 = 12.7\,\mathrm{kHz}$ [23], producing the 1QC and the 2QC interferograms upon demodulation, respectively. Finally, a Fourier transform of the interferograms, oscillating against τ at the atomic $D_{1,2}$ transition frequencies $\omega_{1,2}$, and at their additive combinations $2\omega_{1,2}$ and $\omega_1 + \omega_2$, yields the 1QC and 2QC spectra, respectively.

Theoretical analysis.— The MQC signals are theoretically modeled by a master equation ansatz describing randomly oriented atomic dipoles which interact through their common electromagnetic environment [28, 29], where we built in the internal structure of the experimentally probed potassium atoms [30] (cf. Fig. 1(a)).

In accordance with the experimental protocol, we seek the total far-field fluorescence intensity emitted into a solid angle Ω around the unit vector $\hat{\mathbf{k}}$ pointing towards the detector, during one excitation/detection cycle of duration T_{cyc} [29]:

$$I_{\Delta\hat{\mathbf{k}}}(T_{\text{cyc}};\tau) = \int_0^{T_{\text{cyc}}} \int dt \, d\Omega \, \langle \mathbf{E}_{\hat{\mathbf{k}}}^{(-)}(t;\tau) \cdot \mathbf{E}_{\hat{\mathbf{k}}}^{(+)}(t;\tau) \rangle, (1)$$

where $\mathbf{E}_{\hat{\mathbf{k}}}^{(\pm)}(t;\tau)$ is the positive/negative frequency part of the electric field operator, which can be expressed in terms of the atomic dipole operators and implies a summation over all populated polarization channels. $\langle \ldots \rangle$ denotes the quantum mechanical expectation value [23]. The correlator under the integral in Eq. (1) is deduced from the solution of the master equation for three randomly placed (at distances much larger than the wave length associated with the atomic transition frequency)

and oriented K atoms, each initially uniformly populating the ground state's Zeeman sublevels. We exploit the separation of the time scales of the problem [29]: During the action of the ultrashort pulses, radiative decay and dipole-dipole interactions are neglected. Beyond these times, pairwise dipole-dipole interactions are treated perturbatively, at lowest (second) order in the interaction tensor **T** (see below), which survives the average over the atoms' random positions [29, 31, 32]. Consequently, recurrent scattering whereupon a photon bounces back and forth between the same pair of coupled atoms is neglected [29].

To account for the pulsed excitation, we use a simplified scheme with two, instead of four, pulses, which however captures all relevant features of the experiment [23]. The pulses are modeled as delta pulses with identical pulse areas [33], and their (near-resonant) interaction with the atoms is treated *non-perturbatively* (in the sense of admitting saturation effects). Laser pulse j (j = 1, 2) imprints the instantaneous phases $\varphi_i^{(\alpha)} = \mathbf{k}_{\mathbf{L}} \cdot \mathbf{r}_{\alpha 0} + \omega_1 t_j +$ $\Omega_j \tau_m + \Delta_\alpha t_j$ and $\phi_i^{(\alpha)} = \mathbf{k}_L \cdot \mathbf{r}_{\alpha 0} + \omega_2 t_j + \Omega_j \tau_m + \Delta_\alpha t_j$ upon the dipole transitions D_1 and D_2 of atom α , respectively, with $\mathbf{r}_{0\alpha}$ the initial position of the atom at the beginning of cycle m, k_L the driving field wave vector, $\tau_m = mT_{\rm cyc}$, and $\Delta_{\alpha} = \mathbf{k}_{L} \cdot \mathbf{v}_{\alpha}$ the Doppler shift of the atom when moving with velocity \mathbf{v}_{α} [34]. Furthermore, the spectrally broad pulses induce atomic fine-structure coherence (see red dotted arrow in Fig. 1(a)), whose implication is discussed later. After the two pulses, the populations of the $m=\pm 1/2$ sublevels of level $4^2P_{1/2}$ $(4^2P_{3/2})$ carry the position-independent phase $\varphi_{21}^{(\alpha)} = \varphi_{2}^{(\alpha)} - \varphi_{1}^{(\alpha)}$ $(\varphi_{21}^{(\alpha)} = \varphi_{2}^{(\alpha)} - \varphi_{1}^{(\alpha)})$, which identifies the 1QC signal at $\omega_1 \ (\omega_2) \ [35].$

To emit 2QC signals, atoms that have interacted with the laser must also interact twice with each other [29]. The resonant dipole-dipole interaction Liouvillian is proportional to the 3×3 tensor \mathbf{T} , with Cartesian components [23]

$$(\mathbf{T})_{kl} = \frac{3\gamma}{4} \frac{\exp\{ik_0 r_{\alpha\beta}(t)\}}{k_0 r_{\alpha\beta}(t)} \left[(\delta_{kl} - (\hat{\mathbf{n}})_k (\hat{\mathbf{n}})_l) + (\delta_{kl} - 3(\hat{\mathbf{n}})_k (\hat{\mathbf{n}})_l) \left(\frac{i}{k_0 r_{\alpha\beta}(t)} - \frac{1}{(k_0 r_{\alpha\beta}(t))^2} \right) \right],$$
(2)

 $r_{\alpha\beta}(t) = |\mathbf{r}_{0\alpha} - \mathbf{r}_{0\beta} + (\mathbf{v}_{\alpha} - \mathbf{v}_{\beta}) t|$, $\hat{\mathbf{n}}$ the unit vector connecting atoms α and β , $\gamma = 1/\tau_{\rm spon}$ the spontaneous decay rate of either one of the excited states of the D_1 and D_2 transitions, and $k_0 = (\omega_1 + \omega_2)/2c$ the mean of the wave numbers associated with the atomic transition frequencies. \mathbf{T} quantifies the coupling amplitude of the field emitted by one dipole to another dipole [36]; it mediates the retarded dipolar interaction for a broad range of interatomic separations. While most studies dedicated to MQC signals [7–12, 37] account only for the electrostatic, or near-field, dipolar interactions scaling as $\sim r_{\alpha\beta}^{-3}$,

our present results are obtained by retaining the full form (2) of **T**, thereby incorporating the far field interactions. These, scaling as $\sim r_{\alpha\beta}^{-1}$, mediate multiple scattering processes [28, 31, 32].

Robust double scattering contributions to experimental observables stem from products of interaction amplitudes proportional to $(\mathbf{T})_{kl}(t')$ and $(\mathbf{T}^*)_{nm}(t'')$, respectively, at distinct times $0 < t', t'' \sim \tau_{\rm spon}$, which survive the disorder average [38]. For such terms, the exponential phase factors of $(\mathbf{T})_{kl}(t')$ and $(\mathbf{T}^*)_{nm}(t'')$ (see eq. (2)) must approximately compensate each other. This implies that the atomic velocities of the interacting atoms must obey the inequality $|\mathbf{v}_{\alpha} - \mathbf{v}_{\beta}| \tau_{\text{spon}} \ll \lambda$, which is the condition for the atoms to be in the same velocity class. Although it was argued earlier that 2QC signals in a dilute thermal gas originate from interacting atoms which move with near-vanishing relative velocity [37], this requirement was then inferred from the $r_{\alpha\beta}^{-3}(t)$ -dependence of the electrostatic dipolar interactions [37], without account of the indispensable disorder average over the atomic positions. It is the robustness with respect to the latter which we here identify as the actual cause for 2QC signals to survive. Finally, we only retain the resonant interactions between the same dipole transitions of distinct atoms (that is, D_1 - D_1 and D_2 - D_2); the off-resonant dipolar interactions yield terms that oscillate at frequency $\simeq |\omega_1 - \omega_2| \approx 1.73 \,\mathrm{THz}$, and effectively average out during the cycle duration [39].

The fluorescence signal of interacting atoms α and β satisfying the above conditions is modulated by phases $\varphi_{21}^{(\alpha)} + \varphi_{21}^{(\beta)}$ and $\varphi_{21}^{(\alpha)} + \varphi_{21}^{(\beta)}$. Upon demodulation, this gives rise to 2QC signals at $2\omega_1$ and $2\omega_2$, i.e., to the $2D_1$ and $2D_2$ resonances. However, this does not explain the previous observations of cross resonances D_1D_2 [7, 9–11, 14]. These peaks emerge due to the interplay between fine-structure coherence and dipolar interactions, which gives rise to a modulation of the excited state populations by the phases $\varphi_{21}^{(\alpha)} + \varphi_{21}^{(\beta)}$ and $\varphi_{21}^{(\alpha)} + \varphi_{21}^{(\beta)}$. These phases then bring about the cross resonance D_1D_2 , at $\omega_1 + \omega_2$. Note that, if only one of the two dipole-dipole interacting atoms has been excited by the laser pulses, a contribution to the respective 1QC signal due to double scattering appears. In general, a κ QC signal can feature contributions from $s \geq \kappa$ particles, combining 2(s-1) interaction amplitudes.

To summarize, the spectra $\tilde{I}_{1,\Delta\hat{\mathbf{k}}}(\omega)$ and $\tilde{I}_{2,\Delta\hat{\mathbf{k}}}(\omega)$, respectively, of the 1QC and 2QC signals emitted into a solid angle around $\hat{\mathbf{k}}$, can be expanded into a series:

$$\tilde{I}_{1,\Delta\hat{\mathbf{k}}}(\omega) = \tilde{I}_{1,\Delta\hat{\mathbf{k}}}^{[0]}(\omega) + \tilde{I}_{1,\Delta\hat{\mathbf{k}}}^{[2]}(\omega) + \tilde{I}_{1,\Delta\hat{\mathbf{k}}}^{[4]}(\omega) + \dots, \ \ (3\mathrm{a})$$

$$\tilde{I}_{2,\Delta\hat{\mathbf{k}}}(\omega) = \tilde{I}_{2,\Delta\hat{\mathbf{k}}}^{[2]}(\omega) + \tilde{I}_{2,\Delta\hat{\mathbf{k}}}^{[4]}(\omega) + \dots, \tag{3b}$$

where the super-(sub-)scripts indicate the number of involved dipole interaction amplitudes (the order κ of the MQC signal emitted into a solid angle around $\hat{\mathbf{k}}$).

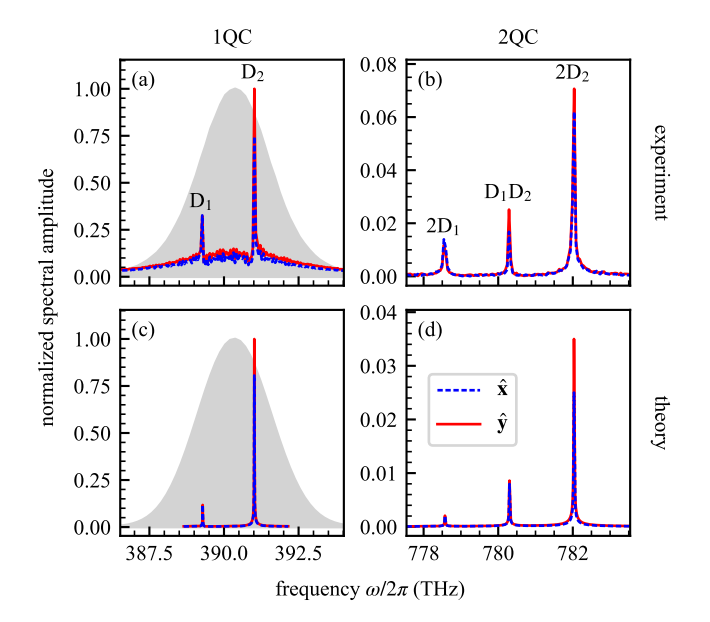


Figure 2. Experimental (a,b) vs. theoretical (c,d) 1QC and 2QC spectra, for detection in the $\hat{\mathbf{x}}$ - (blue) and $\hat{\mathbf{y}}$ -direction (red), respectively, with respect to the injected laser polarization (compare Fig. 1(c,e)) and spectrum (gray). The broad background in (a) is due to stray light. The broader linewidths in the experiment reflect the experimental detector response function. The theoretical spectra are rescaled as described in the main text, with $N_{\rm det}=10^9,\ k_0=8.18\times10^4$ m⁻¹, and $\bar{r}=7.5$ mm.

Spectra and anisotropy of MQC signals.— In Fig. 2(a,b), we present examples of the measured 1QC and 2QC spectra that are normalized by $|\tilde{I}_{1,\Delta\hat{\mathbf{v}}}(\omega_2)|$, for detection parallel ($\hat{\mathbf{x}}$, blue dashed) and perpendicular ($\hat{\mathbf{y}}$, red solid) to the injected polarization direction. The experimental spectra exhibit two and three resonances for 1QC and 2QC spectra, respectively, as anticipated above; they are similar to the previously reported observations [7, 9, 11, 12, 14, 40], and are in good qualitative agreement with our theoretical results (see Fig. 2(c,d)). In theory and experiment, the D₂ and 2D₂ resonances are stronger than the D_1 and $2D_1$ resonances, respectively, due to the larger oscillator strength of the D₂ transition [41]. However, the magnitude of the computed peak originating from the D_2 transition, relative to that of the D_1 line, is several times too strong compared to the measured one. We attribute this to photon frequency redistribution in a thermal vapor [42], which leads to a stronger attenuation of the field in resonance with the D_2 rather than with the D₁ transition (due to the larger scattering cross section of the D_2 transition [43]), but is not accounted for by our model.

Let us now assess the specific role of the retarded part of the dipole-dipole interaction (2) for the observed 1QC and 2QC signals. First, consider the different amplitudes of the 1QC and 2QC spectra. For a quantitative comparison between experiment and theory, we extrapolate

the results of our toy model of three atoms to the bulk vapor. Given the density of the particles and the parameters of the detection system [44], the number of particles in the detection volume is estimated as $N_{\rm det} \sim 10^8 - 10^9$ [44]. Using this, we rescale the single, double, and triple scattering terms (that is, with the superscript [0], [2], and [4], respectively) in Eq. (3) by N_{det} , $N_{\text{det}}^2/(k_0\bar{r})^2$, and $N_{\rm det}^3/(k_0\bar{r})^4$, respectively, where $\bar{r}=0.554n_{\rm vc}^{-1/3}\sim$ 0.6-1.2 cm is the average distance between the particles belonging to the same velocity class, estimated from their density $n_{\rm vc}$ [23, 45]. The thus obtained spectra, normalized by the rescaled value of $|I_{1,\Delta\hat{\mathbf{y}}}(\omega_2)|$, are plotted in Fig. 2(c,d). The relative 1QC/2QC magnitudes of the D₂ and 2D₂ peaks retrieved from the calculations and measurements are ≈ 28 and ≈ 13 , respectively. Note that this result clearly improves over that obtained when only the static (i.e., non-retarded) part of the dipole-dipole interaction is accounted for, leading to an overestimation of the 1QC/2QC amplitude ratio by a factor 10⁷ [9], with respect to the values here obtained.

We remark that the relatively strong 2QC signals cannot be explained by semiclassical theory of multiple scattering [46], which describes the propagation of a photon as a random walk. One of the key parameters describing the walk is the photon scattering mean free path ℓ . For the considered vapor densities, $\ell \gtrsim 1 \text{ m} \gg L = 5 \text{ cm}$ (see above) [47], such that photons should travel quasiballistically across so optically thin vapor, with, at most, one scattering event [48]. Hence, 2QC signals should not be observed, else their magnitude should be negligible compared to 1QC signals. This contradicts our observations, and it is known that the random-walk model ignores collective effects [49], nor can it accurately describe the fluorescence emission by thermal quantum scatterers in the transverse direction, while the coupled-dipole model succeeds in this task [50].

Another feature of the MQC signals characteristic of both, the measured and the calculated spectra, are the (un)equal amplitudes of the spectral peaks A_x and A_y associated with the D_1 (D_2) transitions in $\hat{\mathbf{x}}$ and $\hat{\mathbf{y}}$ directions (see Fig. 2). We examined this (an)isotropy further by looking at the peak ratios along the two observation directions $\hat{\mathbf{x}}$ and $\hat{\mathbf{y}}$. The bars of the histogram in Fig. 3 present the experimental and theoretical values of the peak ratios, for the five peaks exhibited jointly by 1QC and 2QC spectra. For each peak, we furnish two theoretical bars: one evaluated using the full dipole interaction (2), including the far-field contributions, and the other one retaining solely the electrostatic interactions, which hitherto were almost exclusively used in theoretical treatments of MQC signals in alkali atom vapors.

As expected, the D₁ and 2D₁ peaks (see Fig. 3) exhibit isotropy of the spontaneous emission $(A_y/A_x \approx 1)$ from the excited state's Zeeman sublevels which are equally populated by the linearly polarized pulses (see

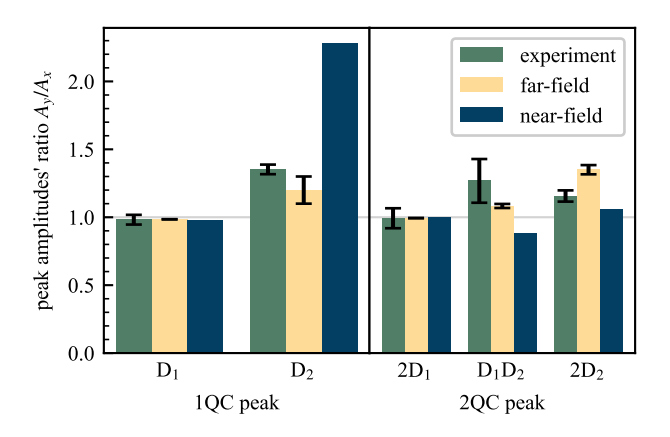


Figure 3. Anisotropy of experimental vs. theoretical 1QC and 2QC signals, the latter derived either from the electrostatic near-field contribution to the dipole-dipole interaction (2) alone, or accounting also for the far-field contributions. Error bars indicate standard deviations for the experimental record, and uncertainties of $N_{\rm det}$ and \bar{r} , for theory (see main text).

Fig. 1(b,c) and [23]). Conversely, peaks involving D_2 transitions are anisotropic. The computed 1QC D_2 signal exhibits the ratio $A_y/A_x = 1.2(1)$, which is in reasonably good agreement with the experimental observation $(A_y/A_x = 1.35(4))$. These values are significantly smaller than the ratio $A_y/A_x \approx 2.25$ characteristic of independent atoms [23], or than the value $A_y/A_x \approx 2.28$ derived by us for a system of atoms coupled by the near-field interaction alone. Thus, the reduced anisotropy of 1QC signals stems from the redistribution of Zeeman level populations mediated by the far-field dipole-dipole interactions. This conclusion is further corroborated by the anisotropy of 2QC signals involving the D₂ transition. The far-field dipolar contributions yield signal ratios $A_y/A_x > 1$ of the 2D₂ and D₁D₂ peaks, respectively, in qualitative agreement with experiment, while the electrostatic interactions alone, in contrast, result invert this ratio, for the D_1D_2 peak (see Fig. 3). Finally, we note that population redistribution may also be mediated by thermal atomic collisions. However, in our manybody system, interatomic collisions occur on a time scale $\tau_{\rm coll} \sim 1.5\,{\rm ms} \gg \tau_{\rm spon} \approx 26\,{\rm ns}$ [23], and are thus not relevant for the MQC signals.

Conclusion.— Our experimental results and theoretical analysis of the amplitude ratio between 1QC and 2QC signals and their anisotropy in very dilute thermal vapors of alkali atoms provide clear evidence of the far-field dipole-dipole interactions as the physical mechanism underlying MQC signals. The interatomic interactions persist for quantum emitters moving very slowly relative to each other, and the MQC detection scheme extracts their signatures despite strong inhomogeneous broadening. The ability of this technique to detect weak inter-

actions without the need for confined geometries [18, 21] paves a promising way towards the sensing and control of dilute thermal systems.

We thank U. Bangert and I.M. Sokolov for insightful discussions. This work was supported by the European Research Council (ERC) with the Advanced Grant COCONIS (694965), by the German Research Foundation (DFG; IRTG 2079, RTG 2717), and by the state of Baden-Württemberg through bwHPC. V. S. and A. B. acknowledge partial funding and support through the Strategiefonds der Albert-Ludwigs-Universität Freiburg and the Georg H. Endress Stiftung.

- * vyacheslav.shatokhin@physik.uni-freiburg.de
- [1] R. H. Dicke, Physical Review **93**, 99 (1954).
- [2] M. J. Stephen, The Journal of Chemical Physics 40, 669 (1964).
- [3] D. A. Hutchinson and H. F. Hameka, The Journal of Chemical Physics 41, 2006 (1964).
- [4] M. Gross and S. Haroche, Physics Reports 93, 301 (1982).
- [5] S. D. Jenkins, J. Ruostekoski, J. Javanainen, R. Bourgain, S. Jennewein, Y. R. P. Sortais, and A. Browaeys, Physical Review Letters 116, 183601 (2016).
- [6] S. Mukamel, The Journal of Chemical Physics 145, 041102 (2016).
- [7] X. Dai, M. Richter, H. Li, A. D. Bristow, C. Falvo, S. Mukamel, and S. T. Cundiff, Physical Review Letters 108, 193201 (2012).
- [8] F. Gao, S. T. Cundiff, and H. Li, Optics Letters 41, 2954 (2016).
- [9] L. Bruder, A. Eisfeld, U. Bangert, M. Binz, M. Jakob, D. Uhl, M. Schulz-Weiling, E. R. Grant, and F. Stienkemeier, Physical Chemistry Chemical Physics 21, 2276 (2019).
- [10] S. Yu, M. Titze, Y. Zhu, X. Liu, and H. Li, Optics Express 27, 28891 (2019).
- [11] S. Yu, M. Titze, Y. Zhu, X. Liu, and H. Li, Optics Letters 44, 2795 (2019).
- [12] D. Liang and H. Li, The Journal of Chemical Physics 154, 214301 (2021).
- [13] F. Landmesser, T. Sixt, K. Dulitz, L. Bruder, and F. Stienkemeier, Optics Letters 48, 473 (2023).
- [14] L. Bruder, M. Binz, and F. Stienkemeier, Physical Review A 92, 053412 (2015).
- [15] D. Pizzey, J. D. Briscoe, F. D. Logue, F. S. Ponciano-Ojeda, S. A. Wrathmall, and I. G. Hughes, New Journal of Physics 24, 125001 (2022).
- [16] A. Fabricant, I. Novikova, and G. Bison, New Journal of Physics 25, 025001 (2023).
- [17] D. Uhland, H. Dillmann, Y. Wang, and I. Gerhardt, New Journal of Physics 25, 125001 (2023).
- [18] A. Skljarow, H. Kübler, C. S. Adams, T. Pfau, R. Löw, and H. Alaeian, Physical Review Research 4, 023073 (2022).
- [19] G. Buser, R. Mottola, B. Cotting, J. Wolters, and P. Treutlein, PRX Quantum 3, 020349 (2022).
- [20] Q. Glorieux, T. Aladjidi, P. D. Lett, and R. Kaiser, New Journal of Physics 25, 051201 (2023).

- [21] H. Alaeian, A. Skljarow, S. Scheel, T. Pfau, and R. Löw, New Journal of Physics 26, 055001 (2024).
- [22] Resonance frequencies of $4^2S_{1/2} \rightarrow 4^2P_{1/2}$ and $4^2S_{1/2} \rightarrow 4^2P_{3/2}$ transitions are $\omega_1 = 2\pi \times 389.6 \,\text{THz}$ (D₁) and $\omega_2 = 2\pi \times 391.3 \,\text{THz}$ (D₂).
- [23] See Supplemental Material at www, which includes further details on the measurement of MQC signals and further details.
- [24] P. F. Tekavec, T. R. Dyke, and A. H. Marcus, The Journal of Chemical Physics 125, 194303 (2006).
- [25] M. Binz, L. Bruder, L. Chen, M. F. Gelin, W. Domcke, and F. Stienkemeier, Opt. Express 28, 25806 (2020).
- [26] U. Bangert, L. Bruder, and F. Stienkemeier, Optics Letters 48, 538 (2023).
- [27] A. Hedse, A. A. S. Kalaee, A. Wacker, and T. Pullerits, The Journal of Chemical Physics 158, 141104 (2023).
- [28] V. Shatokhin, C. A. Müller, and A. Buchleitner, Physical Review Letters 94, 043603 (2005).
- [29] B. Ames, E. G. Carnio, V. N. Shatokhin, and A. Buchleitner, New Journal of Physics 24, 013024 (2022).
- [30] The hyperfine structure is neither resolved in the experiment nor included in our theoretical description.
- [31] A. Ketterer, A. Buchleitner, and V. N. Shatokhin, Phys. Rev. A 90, 053839 (2014).
- [32] T. Binninger, V. N. Shatokhin, A. Buchleitner, and T. Wellens, Physical Review A 100, 033816 (2019).
- [33] The results of the two pulse excitation are equivalent to the four pulse results, upon rescaling [23].
- [34] Our results are averaged over the Maxwell-Boltzmann distribution of Δ_{α} .
- [35] B. Ames, A. Buchleitner, E. G. Carnio, and V. N. Shatokhin, The Journal of Chemical Physics 155, 044306 (2021).
- [36] L. D. Landau and E. M. Lifshitz, The classical theory of fields, 4th ed. (Pergamon Press, Oxford, 1987).
- [37] B. Lomsadze and S. T. Cundiff, Physical Review Letters 120, 233401 (2018).
- [38] In some analogy to robust against disorder averaging interference contributions which give rise to the coherent backscattering signal upon multiple scattering of light off clouds of cold atoms (see [28, 32], and references therein).
- [39] R. R. Puri, Mathematical Methods of Quantum Optics (Springer, Berlin, 2001).
- [40] L. Bruder, U. Bangert, and F. Stienkemeier, Optics Express 25, 5302 (2017).
- [41] D. A. Steck, "Quantum and Atom Optics," available online at http://steck.us/teaching (2022-07-28).
- [42] A. F. Molisch and B. P. Oehry, Radiation Trapping in Atomic Vapours (Clarendon Press, Oxford, 1998).
- [43] D. Budker, D. F. Kimball, and D. P. DeMille, Atomic physics: An exploration through problems and solutions, 2nd ed. (Oxford University Press, Oxford, 2008).
- [44] F. Landmesser, Multiple-quantum coherence spectroscopy of alkali ensembles in the gas phase, Dissertation, Albert-Ludwigs-Universität, Freiburg im Breisgau (2024).
- [45] S. Chandrasekhar, Rev. Mod. Phys. **15**, 1 (1943).
- [46] A. Lagendijk and B. A. van Tiggelen, Physics Reports **270**, 143 (1996).
- [47] G. Di Domenico and A. Weis, "Spectra of the D-Lines of Alkali Vapors," Wolfram Demonstrations Project. demonstrations.wolfram.com/SpectraOfTheDLinesOfAlkaliVapors/ (2011).
- [48] N. Mercadier, W. Guerin, M. Chevrollier, and R. Kaiser,

- Nature Physics 5, 602 (2009).
- [49] I. M. Sokolov and W. Guerin, J. Opt. Soc. Am. B 36, 2030 (2019).
- [50] S. L. Bromley, B. Zhu, M. Bishof, X. Zhang, T. Bothwell, J. Schachenmayer, T. L. Nicholson, R. Kaiser, S. F. Yelin, M. D. Lukin, A. M. Rey, and J. Ye, Nature Communications 7, 11039 EP (2016).
- [51] V. A. Osipov and T. Pullerits, Phys. Rev. A 96, 043841 (2017).
- [52] W. Happer, Y.-Y. Jau, and T. Walker, Optically Pumped Atoms (Wiley-VCH Verlag, Winheim, 2019).
- [53] E. Clementi, D. L. Raimondi, and W. P. Reinhardt, The Journal of Chemical Physics 47, 1300 (1967).
- [54] C. B. Alcock, V. P. Itkin, and M. K. Horrigan, Canadian Metallurgical Quarterly 23, 309 (1984).
- [55] H. Wang, P. L. Gould, and W. C. Stwalley, The Journal of Chemical Physics 106, 7899 (1997).

SUPPLEMENTAL MATERIAL

Accumulation effects

In the experiment, the time interval $T_{\rm cyc} \approx 10$ ns between consecutive laser cycles is of the order of the natural lifetime $\tau_{\rm spon} \approx 26$ ns, which in principle can lead to the accumulation of spurious nonlinear signals over several laser cycles [51]. We overcome this problem by employing four laser pulses, where each pulse interacts only once with the vapor. Thereby, the system remains in a coherent superposition state during each of the time intervals t_{01} , t_{12} , t_{23} (see the main text). Hence, contributions involving multiple laser cycles are not detected in the four-pulse scheme, since the (multi)atomic coherences decay significantly faster (on a time scale $< 1\,\mathrm{ns}$) than populations, due to the ensemble inhomogeneity.

An analogous detection scheme can be implemented with only two laser pulses which interact multiple times with the system [14]. However, in this case the time interval $T_{\rm cyc}$ between consecutive laser cycles should be taken $\gg \tau_{\rm spon}$, which ensures the absence of artifacts from accumulation over multiple laser cycles. Thus, a two-pulse scheme with $T_{\rm cyc} \gg \tau_{\rm spon}$ is well justified for the theoretical description of the experiment. Furthermore, the results of the two excitations can be mapped onto those of the four-pulse excitation, upon a simple rescaling. Indeed, we have checked that for 1QC signals, the two-pulse excitation produces the same peak amplitudes as the four-pulse excitation. However, for 2QC signals, only the amplitude of the cross peak in the two- and four-pulse excitation setup is the same, whereas the amplitudes of the 2D₁ and 2D₂ peaks in the four-pulse scheme are twice as large. The difference stems from the larger number of processes that contribute to the 2D₁ and 2D₂ peaks in the four-pulse excitation scheme (see Table I). Therefore, the results of the two-pulse excitation coincide with those of the four-pulse excitation, after multiplying by two the amplitudes of the 2D₁ and 2D₂ signals.

Table I. Peaks of the 2QC spectra and the relevant modulation phases in the case of the two- and four-pulse excitation. The phases are introduced in the main text, see also Eq. (8) below.

Peak	Modulation phases					
	2 pulses	4 pulses				
$2D_1$ $2D_2$ D_1D_2	$\varphi_{21}^{(\alpha)} + \varphi_{21}^{(\beta)}$ $\varphi_{21}^{(\alpha)} + \varphi_{21}^{(\beta)}$ $\varphi_{21}^{(\alpha)} + \varphi_{21}^{(\beta)}, \phi_{21}^{(\alpha)} + \varphi_{21}^{(\beta)}$	$\begin{array}{l} \varphi_{30}^{(\alpha)} + \varphi_{21}^{(\beta)}, \varphi_{30}^{(\beta)} + \varphi_{21}^{(\alpha)} \\ \phi_{30}^{(\alpha)} + \phi_{21}^{(\beta)}, \phi_{30}^{(\beta)} + \phi_{21}^{(\alpha)} \\ \varphi_{30}^{(\alpha)} + \phi_{21}^{(\beta)}, \varphi_{30}^{(\beta)} + \phi_{21}^{(\alpha)} \end{array}$				

Fluorescence anisotropy

Figure 4 provides an intuitive explanation for the observed anisotropy in the fluorescence emission. The atoms are excited by a sequence of laser pulses linearly polarized along the $\hat{\mathbf{x}}$ -axis, inducing π -transitions ($\Delta m = 0$) in the atoms (red arrows). Fluorescence emission, which occurs through atomic π - and σ -transitions ($\Delta m = \pm 1$), exhibits an angular distribution of intensity of linearly and circularly polarized light characterized by the corresponding Clebsch-Gordon coefficients (see Fig. 4). The total intensity, summed over all polarizations, is isotropic for the D₁ line and anisotropic for the D₂ line. Note that for an isolated atom, the sublevels with $m = \pm 3/2$ will not be excited by linear polarized light. However, the dipolar interactions between the atoms can lead to excitation of these sublevels, which will effectively reduce the anisotropy of the D₂ and 2D₂ signals, as we observed in the experiment.

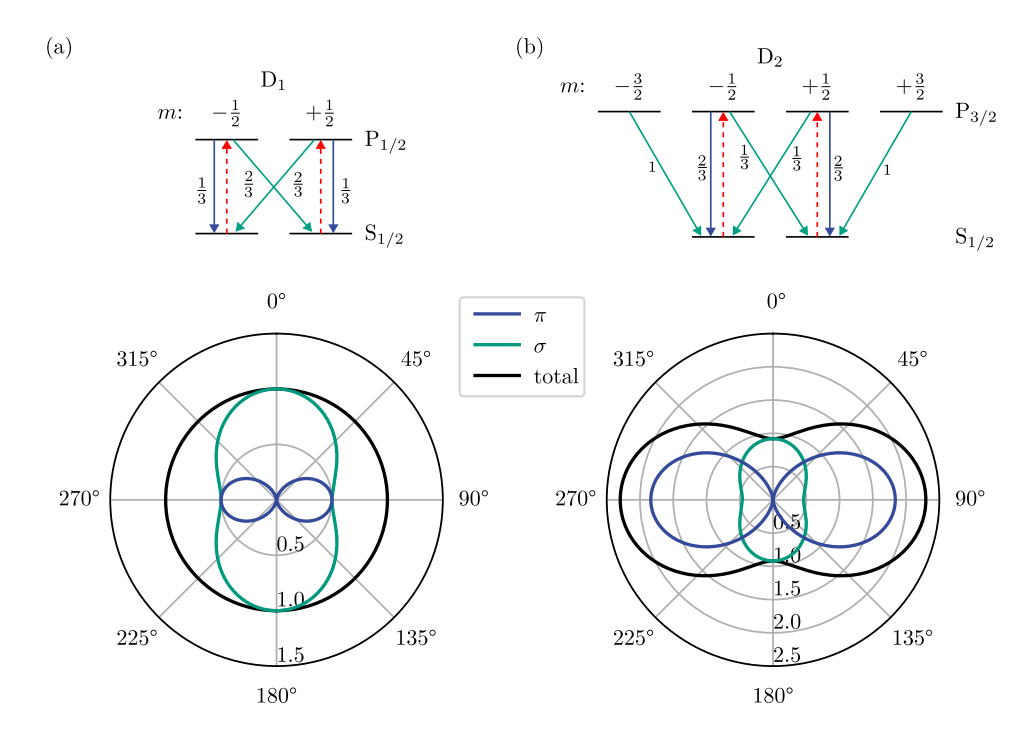


Figure 4. Angular distribution of fluorescence emission from an isolated alkali atom via the D₁ (a) and D₂ (b) transitions. Top: Fine structure level scheme with degenerate magnetic sublevels (m) and the squared Clebsch-Gordan coefficients for each transition. Dashed red lines indicate the linearly polarized laser excitation, blue arrows the π emission and green arrows the σ emission, respectively. Bottom: The corresponding angular intensity distribution w.r.t. the light's polarization direction x (0°) . The total intensity (black) corresponds to the sum of the two polarization contributions π (blue) and σ (green).

Theoretical description

Spontaneous emission of alkali atoms. — The positive frequency part of the far-field electric field operator of the light spontaneously emitted by atoms in Eq. (1) of the main text is given by the expression [29]

$$\mathbf{E}_{\hat{\mathbf{k}}}^{(+)}(t) \approx \frac{\omega_0 d}{4\pi\epsilon_0 c^2 R} \sum_{\alpha=1}^{N} \left\{ \mathbf{D}_{\alpha}(t) - \hat{\mathbf{k}} [\hat{\mathbf{k}} \cdot \mathbf{D}_{\alpha}(t)] \right\} e^{-i\mathbf{k} \cdot \mathbf{r}_{\alpha}},\tag{4}$$

where $\mathbf{D}_{\alpha}(t) = (\mathbf{D}_{\frac{1}{2},\alpha} + \mathbf{D}_{\frac{3}{2},\alpha})$ is the lowering part of the vector atomic dipole operator $\boldsymbol{\mathcal{D}}_{\alpha}(t) = (\mathbf{D}_{\alpha}(t) + \mathbf{D}_{\alpha}^{\dagger}(t))$, and $\mathbf{D}_{\frac{1}{2},\alpha}$ ($\mathbf{D}_{\frac{3}{2},\alpha}$) is the lowering operator associated with the transition D_1 (D_2); scalar d is expressed through the reduced matrix elements as $d \equiv \langle J_{\frac{1}{2}} || \mathbf{D}_{\frac{1}{2}} || J_{\frac{1}{2}} \rangle / \sqrt{2} \approx \langle J_{\frac{1}{2}} || \mathbf{D}_{\frac{3}{2}} || J_{\frac{3}{2}} \rangle / 2$ [41], $\omega_0 = (\omega_1 + \omega_2)/2$, c is the speed of light, and R is the distance from each atom to the detector. The prefactor $\omega_0 d/(4\pi\epsilon_0 c^2 R)$ ignores the difference between the transition frequencies of the D₁ and D₂ transitions (however, this difference is crucial for, and is retained in, the phase factors $\varphi_j^{(\alpha)}$ and $\phi_j^{(\alpha)}$ defined in the main text) and the variation of the distances from individual atoms to the detector. The lowering operator $\mathbf{D}_{J_{\mathrm{e}}}$ of a transition with the total angular momentum of the excited state J_{e} reads (we drop index α for brevity)

$$\mathbf{D}_{J_{e}} = \sum_{q=-1}^{+1} \sum_{m_{g}=-J_{g}}^{J_{g}} (-1)^{q} \hat{\mathbf{e}}_{q} \langle J_{g} m_{q}, 1q | J_{e} m_{g} + q \rangle |J_{g} m_{g} \rangle \langle J_{e} m_{g} + q |,$$
 (5)

where $\hat{\mathbf{e}}_q$ is the unit vector in the spherical basis and $\langle J_{\mathrm{g}} m_q, 1q | J_{\mathrm{e}} m_{\mathrm{g}} + q \rangle$ is the Clebsch-Gordan coefficient. The fluorescence intensity is proportional to $\langle \mathbf{E}_{\hat{\mathbf{k}}}^{(-)}(t) \mathbf{E}_{\hat{\mathbf{k}}}^{(+)}(t) \rangle$ and, by Eq. (4), depends on N^2 two-atom correlation functions. However, the correlators of different atoms contain position-dependent phases $e^{\pm i\mathbf{k}\cdot(\mathbf{r}_{\alpha}(t)-\mathbf{r}_{\beta}(t))}$. Such terms do not survive the average over the atomic coordinates that needs to be performed in our disordered system; therefore, we drop all terms containing position-depending phases of different atoms. We thus arrive at the expression which

includes a single sum over atomic correlators of all particles [29, 35]:

$$\langle \mathbf{E}_{\hat{\mathbf{k}}}^{(-)}(t)\mathbf{E}_{\hat{\mathbf{k}}}^{(+)}(t)\rangle = f^2 \sum_{J_{\mathrm{e}}=\frac{1}{2},\frac{3}{2}} \sum_{\alpha=1}^{N} \langle \mathbf{D}_{J_{\mathrm{e}},\alpha}^{+}(t') \cdot (\mathbf{I} - \hat{\mathbf{k}}\hat{\mathbf{k}}) \cdot \mathbf{D}_{J_{\mathrm{e}},\alpha}(t)\rangle, \tag{6}$$

where $f^2 = (\omega_0 d)^2/(4\pi\epsilon_0 c^2 R)^2$, **I** is the unit dyadic. Integration of Eq. (6) over the wave vectors $\hat{\mathbf{k}}$ within the solid angle subtended by the detection system and over the fluorescence detection time t yields Eq. (1) of the main text. This expression still depends on position-dependent phases of the same atoms. In the final result, we drop these terms and retain only those terms that do not include any position-dependent phases. These terms yield contributions that are robust under the disorder average [29]. We selected these contributions from the general analytical expression for the fluorescence intensity [29] (also see below).

Master equation. — For the assessment of the atomic correlators in (6), we used a master equation for the quantum mechanical expectation value of an atomic operator Q [29]. In the interaction picture with respect to the Liouvillian of free atoms, $\mathcal{L}_0 = \sum_{\alpha=1}^{N} \mathcal{L}_0^{\alpha}$, the master equation reads [29]:

$$\langle \dot{Q} \rangle = \langle (\mathcal{L}_L + \mathcal{L}_\gamma + \mathcal{L}_{\text{int}}) Q \rangle, \tag{7}$$

where $\mathcal{L}_L = \sum_{\alpha=1}^N \mathcal{L}_L^{\alpha}$, $\mathcal{L}_{\gamma} = \sum_{\alpha=1}^N \mathcal{L}_{\gamma}^{\alpha}$ and $\mathcal{L}_{int} = \sum_{\alpha \neq \beta=1}^N \mathcal{L}_{\alpha\beta}$ are the Liouvillian operators governing the laser-atom interaction, relaxation, and dipole-dipole interactions, respectively. The Liouvillians under the sums read

$$\mathcal{L}_L^{\alpha}Q = -\frac{i\vartheta_0}{2} [\mathbf{D}_{\frac{1}{2},\alpha} \cdot \hat{\mathbf{e}}_L^* e^{-i\varphi_j^{(\alpha)}t_j} + \mathbf{D}_{\frac{3}{2},\alpha} \cdot \hat{\mathbf{e}}_L e^{-i\phi_j^{(\alpha)}t_j} + \text{h.c.}, Q], \tag{8}$$

$$\mathcal{L}_{\gamma}^{\alpha}Q = \frac{\gamma}{2} \left(\mathbf{D}_{\frac{1}{2},\alpha}^{+} \cdot [Q, \mathbf{D}_{\frac{1}{2},\alpha}] + [\mathbf{D}_{\frac{1}{2},\alpha}^{+}, Q] \cdot \mathbf{D}_{\frac{1}{2},\alpha}] \right) + \left(\frac{1}{2} \to \frac{3}{2} \right), \tag{9}$$

$$\mathcal{L}_{\alpha\beta}Q = \left(\mathbf{D}_{\frac{1}{2},\alpha}^{+} \cdot \mathbf{T}^{*}(r_{\alpha\beta}(t),\hat{\mathbf{n}}) \cdot [Q,\mathbf{D}_{\frac{1}{2},\beta}] + [\mathbf{D}_{\frac{1}{2},\beta}^{+},Q] \cdot \mathbf{T}(r_{\alpha\beta}(t),\hat{\mathbf{n}}) \cdot \mathbf{D}_{\frac{1}{2},\alpha}\right) + \left(\frac{1}{2} \to \frac{3}{2}\right),\tag{10}$$

where the atomic dipole operators \mathbf{D}_{J_e} ($J_e = \frac{1}{2}, \frac{3}{2}$) are given by Eq. (5), and tensor \mathbf{T} is defined in Eq. (2) of the main text. Equation (8) describes the Liouvillian of a laser pulse acting upon atom α at time t_j . As mentioned in the main text, we modeled pulses by delta-functions multiplied by the pulse areas. We assume that the carrier frequency of the laser pulses $\omega_L = \omega_0$, such that the resonant field amplitude is the same for transitions D_1 and D_2 . Hence, we apply the same pulse area ϑ_0 for both transitions, while keeping track of the phases $\varphi_j^{(\alpha)}$ and $\phi_j^{(\alpha)}$ imprinted on atomic transitions by the pulses (see the main text). During the action of laser pulses, we ignore the Liouvillians \mathcal{L}_{γ} and \mathcal{L}_{int} and evaluate the unitary rotation of an operator Q by \mathcal{L}_L^{α} non-perturbatively [29]. However, for the pulses' parameters used in the experiment [44](see also the main text)

$$\vartheta_0 \simeq \frac{d}{\hbar} \sqrt{\frac{2I_L}{c\epsilon_0}} \sqrt{\frac{\pi}{2\log(2)}} \sigma \simeq 0.3,$$
(11)

where $I_L \approx 3.5 \,\mathrm{MW \cdot cm^{-2}}$ [44] and $d = 2.46 \times 10^{-29} \,\mathrm{C \cdot m}$ [41]. In this weak driving regime, a perturbative treatment provides quite accurate results [35].

In Eqs. (9), (10), we ignore the small differences (about 1% [41]) in the spontaneous decay rates of the excited states $4^2P_{1/2}$ and $4^2P_{3/2}$, using a single rate γ . Furthermore, note that both, the radiative relaxation Liouvillian $\mathcal{L}_{\gamma}^{\alpha}$ and the dipolar interactions Liouvillian $\mathcal{L}_{\alpha\beta}$ features only resonant terms (that is, D₁-D₁ and D₂-D₂ transitions are coupled). The terms describing the cross coupling D₁-D₂ are not included in our Liouvillians; these terms oscillate at frequency $\omega_2 - \omega_1 \approx 1.73 \,\text{THz}$ and are effectively averaged out during one cycle [39].

We consider N=3 potassium atoms located in the far-field $(k_0r_{\alpha\beta}\gg 1)$ of each other. We assume that only atom α and/or β can interact with the laser field; the third atom is not driven by the laser, but participates in the dipole-dipole interactions. The presence of the third atom allows to improve the agreement with experiment for the anisotropy of 2QC signals, as compared to the two-atom case. We exploit the separation of time scales of the problem [29] and seek time-dependent solutions of Eq. (7) perturbatively up to fourth order in the coupling strength $|\mathbf{T}|$, using the full form of tensor \mathbf{T} . In contrast, the near-field results are derived by retaining only the terms $\sim (k_0 r_{\alpha\beta})^{-3}$.

The results obtained for fixed configurations of atoms contain a tremendous number of terms, but most of them carry position-dependent phases and, hence, they do not survive the disorder average. Robust contributions are selected using the criteria outlined in the main text and Refs. [29, 35]. The angular averages are carried out as described in Refs. [29, 31].

The average time-dependent fluorescence intensity emitted in direction $\hat{\mathbf{k}}$ admits the following expansion:

$$\begin{split} I_{\hat{\mathbf{k}}}(t,\tau) &= \sum_{l=-1}^{+1} \left[(I_{\frac{1}{2}}^{1})_{l,\hat{\mathbf{k}}}^{[0]}(t,\tau) e^{i\varphi_{21}^{(\alpha)}l} + (I_{\frac{1}{2}}^{1})_{l,\hat{\mathbf{k}}}^{[2]}(t,\tau) e^{i\varphi_{21}^{(\alpha)}l} + (I_{\frac{1}{2}}^{1})_{l,\hat{\mathbf{k}}}^{[4]}(t,\tau) e^{i\varphi_{21}^{(\alpha)}l} \right. \\ &+ (I_{\frac{3}{2}}^{1})_{l,\hat{\mathbf{k}}}^{[0]}(t,\tau) e^{i\varphi_{21}^{(\alpha)}l} + (I_{\frac{3}{2}}^{1})_{l,\hat{\mathbf{k}}}^{[2]}(t,\tau) e^{i\varphi_{21}^{(\alpha)}l} + (I_{\frac{3}{2}}^{1})_{l,\hat{\mathbf{k}}}^{[4]}(t,\tau) e^{i\varphi_{21}^{(\alpha)}l} \\ &+ (I_{\frac{1}{2}}^{2})_{l,\hat{\mathbf{k}}}^{[2]}(t,\tau) e^{i(\varphi_{21}^{(\alpha)}+\varphi_{21}^{(\beta)})l} + (I_{\frac{1}{2}}^{2})_{l,\hat{\mathbf{k}}}^{[4]}(t,\tau) e^{i(\varphi_{21}^{(\alpha)}+\varphi_{21}^{(\beta)})l} \\ &+ (I_{\frac{3}{2}}^{2})_{l,\hat{\mathbf{k}}}^{[2]}(t,\tau) e^{i(\varphi_{21}^{(\alpha)}+\varphi_{21}^{(\beta)})l} + (I_{\frac{3}{2},\frac{3}{2}}^{2})_{l,\hat{\mathbf{k}}}^{[4]}(t,\tau) e^{i(\varphi_{21}^{(\alpha)}+\varphi_{21}^{(\beta)})l} \\ &+ (I_{\frac{1}{2},\frac{3}{2}}^{2})_{l,\hat{\mathbf{k}}}^{[4]}(t,\tau) e^{i(\varphi_{21}^{(\alpha)}+\varphi_{21}^{(\beta)})l} + (I_{\frac{1}{2},\frac{3}{2}}^{2})_{l,\hat{\mathbf{k}}}^{[4]}(t,\tau) e^{i(\varphi_{21}^{(\alpha)}+\varphi_{21}^{(\beta)})l} \\ &+ (I_{\frac{1}{2},\frac{3}{2}}^{2})_{l,\hat{\mathbf{k}}}^{[4]}(t,\tau) e^{i(\varphi_{21}^{(\alpha)}+\varphi_{21}^{(\beta)})l} + (I_{\frac{1}{2},\frac{3}{2}}^{2})_{l,\hat{\mathbf{k}}}^{[4]}(t,\tau) e^{i(\varphi_{21}^{(\alpha)}+\varphi_{21}^{(\beta)})l} \right], \end{split}$$

where $(I_{J_e}^{\kappa})_{l,\hat{\mathbf{k}}}^{[2(s-1)]}(t,\tau)$ and $(I_{J_e,J_e'}^{\kappa})_{l,\hat{\mathbf{k}}}^{[2(s-1)]}(t,\tau)$ are contributions to κD_1 , κD_2 peaks (terms with $J_e = \frac{1}{2}$ or $J_e = \frac{3}{2}$) or to the cross peak D_1D_2 (terms with J_e , $J_e' = \frac{1}{2}, \frac{3}{2}$) stemming from s = 1, 2, 3 atoms. The 1QC and 2QC spectra as given in the main text by Eqs. (2a) and (2b), respectively, are obtained via the demodulation procedure, which is compactly expressed by the formula [29]

$$\tilde{I}_{\kappa,\Delta\hat{\mathbf{k}}}(\omega) = \lim_{\mathcal{F}\to 0} \int_0^\infty d\tau_m \ e^{-(\mathcal{F}+i\kappa\Omega_{21})\tau_m} \int_0^\infty d\tau \ e^{-i\omega\tau} \int_0^{T_{cyc}} dt \ \int d\Omega \ I_{\hat{\mathbf{k}}}(t,\tau), \tag{13}$$

where $\Omega_{21} = \Omega_2 - \Omega_1$, \mathcal{F} determines the filter bandwidth to extract the Ω_{21} -modulation, and we set $T_{\rm cyc} \to \infty$ in the calculations (see the justification above).

Averaging the spectra over the Doppler distribution. — We performed the integrations in Eq. (13) analytically, and obtained that the 1QC and 2QC spectra represent Lorentzian peaks. For the 1QC spectra, the two peaks are centered at frequencies $\omega_1 + \Delta_{\alpha}$ and $\omega_2 + \Delta_{\alpha}$; for the 2QC spectra, the peaks are located at frequencies $2(\omega_1 + \Delta_{\alpha})$, $2(\omega_2 + \Delta_{\alpha})$, and $\omega_1 + \omega_2 + 2\Delta_{\alpha}$ (although up to 3 atoms contribute to the spectra, they must belong to the same velocity class in order to yield robust contributions, thus, their Doppler shifts Δ_{α} are the same to a good approximation). We outline how we perform the average of Δ_{α} , by considering only the 2D₂ peak (the procedure is the same for the other peaks). The corresponding spectral function reads

$$S(\omega, \Delta_{\alpha}) = \frac{A}{\gamma + i(\omega - 2(\omega_2 + \Delta_{\alpha}))},\tag{14}$$

where A is a numerical factor (which varies depending on the observation direction and the resonance frequency), and all other quantities are defined in the main text. Integrating (14) over the Maxwell-Boltzmann distribution of Δ_{α} , $p(\Delta_{\alpha}) = \exp(-\Delta_{\alpha}^2/2\bar{\Delta}^2)/(\bar{\Delta}\sqrt{2\pi})$ (here, $\bar{\Delta}$ is the root-mean-square Doppler shift ≈ 770 MHz) we obtain

$$\int_{-\infty}^{\infty} d\Delta_{\alpha} S(\omega, \Delta_{\alpha}) p(\Delta_{\alpha}) = \frac{A\sqrt{\pi}}{4\sqrt{2}\bar{\Delta}} w(z), \tag{15}$$

where $w(z) = \exp(-z^2) \operatorname{erfc}(-iz)$ is the Faddeeva function [52], with $\operatorname{erfc}(x)$ the complementary error function, and $z = (i\gamma - \omega + 2\omega_2)/(2\sqrt{2}\bar{\Delta})$.

Mean distance \bar{r} between atoms from the same velocity class. — To estimate \bar{r} , we use the formula [45]

$$\bar{r} \approx 0.554 \ n_{\rm vc}^{-1/3},$$
 (16)

where $n_{\rm vc}$ is the particle density in the same velocity class. From the main text, the velocities of such particles obey the condition

$$|\mathbf{v}_{\alpha} - \mathbf{v}_{\beta}| \sim \sqrt{3}\Delta v \ll \lambda/\tau_{\text{spon}},$$
 (17)

where Δv is the absolute value of the difference between one velocity component (assumed to be equal for each of the three Cartesian components, hence the prefactor $\sqrt{3}$). The probability to find two particles whose velocity difference lies in the range $(-\Delta v, \Delta v)$ is given by

$$p(\Delta v) = \frac{1}{\sqrt{2\pi}\bar{v}} \int_{-\Delta v}^{\Delta v} \mathrm{d}x \exp(-x^2/(2\bar{v}^2)). \tag{18}$$

Table II. Values used for the estimation of the average interatomic collision time.

species	density [54]	atom radius [53]				
i	$n_i \; ({\rm m}^{-3})$	r_i (m)	$\sigma_{i,\mathrm{K}}~(\mathrm{m}^2)$	$ar{v}_{i,\mathrm{K}} \; (\mathrm{m/s})$	$\gamma_{i,\mathrm{K}}$ (Hz)	$1/\gamma_{i,K}$ (s)
K	5.13×10^{14}		7.42×10^{-19}	565	0.215	4.644
Rb	1.05×10^{16}	2.65×10^{-10}	8.11×10^{-19}	483	4.094	0.244
Cs	3.84×10^{16}	2.98×10^{-10}	9.19×10^{-19}	455	16.051	0.062
	4.94×10^{16}				20.361	0.049
22001	1.01 // 10				20.001	0.010

Using $\bar{v} \approx 247$ m/s, $\lambda = 767$ nm, $\tau_{\rm spon} = 26$ ns, and imposing the condition that during the natural lifetime of the excited state, $\tau_{\rm spon}$, the change in the distance between the interacting particles is in the range $\lambda/50 - \lambda/100$, we obtain $p(\Delta v) \approx 0.0011 - 0.00055$. Then for three components, the probability is $p(\Delta v)^3 \approx 1.3 \times 10^{-9} - 1.67 \times 10^{-10}$. Multiplying by the latter value the particle density in the vapor, we obtain $n_{\rm vc} \approx 666152 - 82803$ m⁻³, which by (16) implies $\bar{r} \approx 0.6 - 1.2$ cm.

Estimation of the average thermal collision rate of atoms. — The collision rate γ_j of a species j in a vapor species i is [43]

$$\gamma_j = \sum_i n_i \sigma_{i,j} \bar{v}_{i,j} \,, \tag{19}$$

with particle densities n_i , average relative velocities $\bar{v}_{i,j}$, and estimated collisional cross sections $\sigma_{i,j} \approx \pi(r_i, +r_j)^2$, where $r_{i,j}$ are calculated atomic radii [53]. The relative velocities are given by $\bar{v}_{i,j} = \sqrt{8k_{\rm B}T/\pi\mu_{i,j}}$ with the Boltzmann constant $k_{\rm B}$, the vapor temperature $T=22\,^{\circ}{\rm C}$, and the reduced masses $\mu_{i,j}=m_im_j/(m_i+m_j)$ (m_i : atomic mass). The particle densities are estimated from the vapor pressures [54]. The collision rate of potassium in the vapor cell containing the species K, Rb, and Cs is

$$\gamma_{\rm K} = \sum_{i=\rm K,Rb,Cs} n_i \sigma_{i,\rm K} \bar{v}_{i,\rm K} \approx 20 \,\mathrm{Hz} \,. \tag{20}$$

The different contributions are listed in Tab. II. The average collision time $1/\gamma_{\rm K}\approx 50\,{\rm ms}$ is about 6 orders of magnitude slower than the natural lifetime of the K $4^2{\rm P}_{3/2}$ level of 26.37 ns [55] and, thus, the influence of collisions on the population redistribution can be neglected.